

# Ray-tracing Arcus in Phase A

Hans M. Günther<sup>a</sup>, C. DeRoo<sup>b</sup>, R. K. Heilmann<sup>a</sup>, E. Hertz<sup>c</sup>, R. K. Smith<sup>c</sup>, J. Wilms<sup>d</sup>, and the Arcus collaboration<sup>1</sup>

<sup>a</sup>Massachusetts Institute of Technology, Cambridge, MA, US

<sup>b</sup>University of Iowa, Iowa city, IA, USA

<sup>c</sup>Smithsonian Astrophysical Observatory, 60 Garden St, Cambridge, MA, US

<sup>d</sup>Friedrich-Alexander-Universität, Erlangen-Nürnberg, DE

## ABSTRACT

Spectroscopy of soft X-rays is an extremely powerful tool to understand the physics of hot plasmas in the universe, but in many cases, such as kinematic properties of stellar emission lines or weak absorption features, we have reached the limits of current instrumentation. Critical-angle transmission (CAT) gratings blaze the dispersed spectra into high orders and also offer high throughput.

We present detailed ray-traces for the Arcus mission, which promises an effective area  $> 300 \text{ cm}^2$  in the soft X-ray band. It uses four petals of Athena-like silicon pore optics. Each petal spans an azimuth of about 30 degrees and thus offers a point-spread function that is significantly narrower in one dimension than a full mirror would provide. Each of these channels has its own optical axis. For each channel, CAT gratings are arranged on a tilted Rowland torus, and the four separate tori are positioned to overlap in such a way that the dispersed spectra from both pairs can be imaged onto a common set of CCD detectors, while at the same time keeping the requirement of the spectroscopic focus.

Our ray-traces show that a set of 16 CCDs is sufficient to cover both zeroth orders and most of the dispersed signal. We study the impact of misalignment, finite size of components, and spacecraft jitter on the spectral resolution and effective area and prove that the design achieves  $R > 3000$  even in the presence of these non-ideal effects.

In 2017, we presented the ray-traces for the initial Arcus proposal. Since then, Arcus was accepted for a phase A study and we have spent a lot of additional effort to tweak the optical design (for example, we originally intended to have two petals each share an optical axis, but decided against it to avoid alignment constraints) and to link it back to practical mechanical engineering tolerances. In the process, parameters that were only roughly known in the initial proposal have been set to much better than a millimeter, and effects that seemed not important initially have now been studied in much more detail. This contribution presents those detailed studies and tells the story how we used ray-traces to make a better instrument with a more robust design.

**Keywords:** ray-tracing, X-ray optics, critical angle transmission grating, ARCUS, Rowland design

## 1. INTRODUCTION

Arcus is a NASA medium explorer (MIDEX) mission that was accepted for a Phase A study in 2017. The mission evolved through several stages. It was originally proposed as an instrument mounted on the International Space Station<sup>1</sup> and then redesigned as a satellite.<sup>2,3</sup> Arcus will do high-resolution spectroscopy in the soft X-ray range (about 12-50 Å) with a resolving power  $R > 3000$  and an effective area  $A_{\text{eff}} > 300 \text{ cm}^2$  for most of the bandpass. The resolving power is a factor of 3 – 5 larger than what existing instruments on Chandra or XMM-Newton can deliver and the effective area is also significantly higher; the exact number depends on the bandpass, e.g. in the crucial region around the O VII He-like triplet, which is density and temperature sensitive, Arcus will reach about two orders of magnitude more effective area than Chandra/HETG currently has.

---

Send correspondence to H.M.G.

E-mail: hgunther@mit.edu

The increase in resolving power, coupled with the increase in effective area, makes new investigations possible e.g. to probe the missing baryons through absorption spectroscopy of the cosmic web, to probe winds from supermassive black holes, again through absorption spectroscopy, and to resolve kinematic structure in the emission lines from young and accreting stars, among other questions.<sup>2-4</sup>

Beginning in the very early phases of the mission design we performed ray-tracing to verify the performance characteristics of Arcus and to improve the design.<sup>5,6</sup>

Ray-trace results for the Arcus configuration proposed to the MIDEX program are shown in reference 7 with a particular emphasis on the boom and any grating misalignment. Since then, minor modifications have been done to the design which we describe in section 2 before we summarize our ray-tracing approach in section 3. We present our extensive ray-tracing results in section 4 and describe how they fit into the end-to-end simulations performed for Arcus (section 5). We end with a short summary in section 6.

## 2. OPTICAL DESIGN OF ARCUS

The optical design of Arcus is described elsewhere,<sup>2,3</sup> and all aspects important to the ray-trace in particular are given in reference 7; see figure 1 for a rendering. Here, we only provide a short summary and highlight changes in the setup compared to our previous ray-tracing paper.<sup>7</sup>

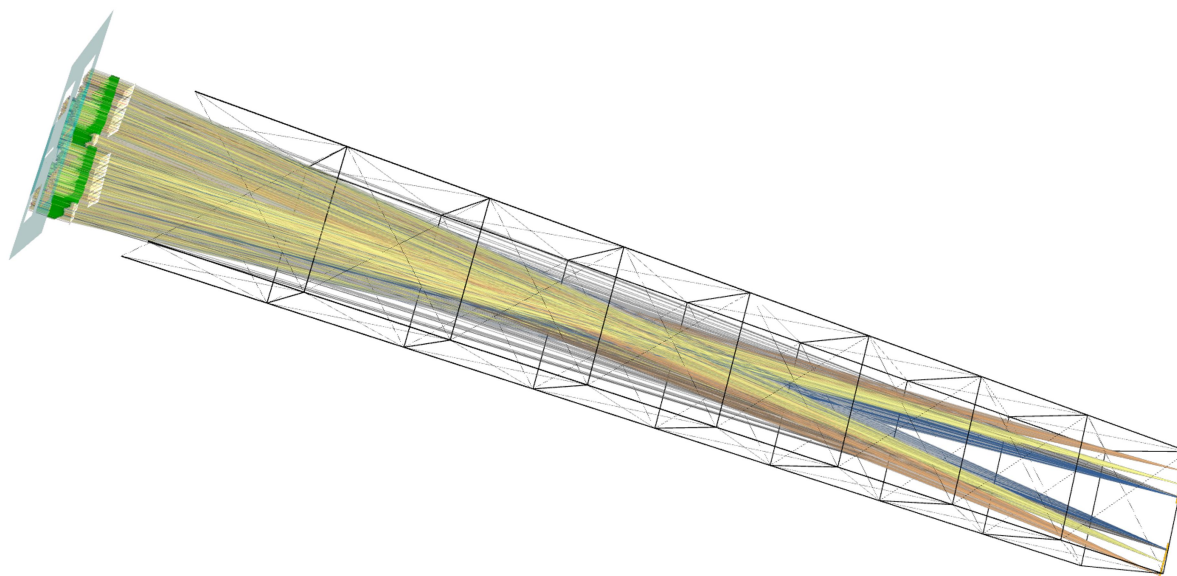


Figure 1. Arcus to scale. On the left are the four channels with SPOs (green) and CAT gratings (white) connected with an extendable boom (black) to the rear assembly where the CCDs (yellow) can be found. Lines show ray-traces for a monoenergetic source. Different colors indicate different diffraction orders. Only rays that reach the detector are shown.

Arcus consists of four channels each of which follows a Rowland-torus design.<sup>8</sup> The mirror is made up of silicon pore optics (SPOs) as developed for Athena.<sup>9,10</sup> For each channel, 34 mirror-modules are mounted in a grating petal. The radius of curvature for the modules is between 320 and 850 mm. Each petal covers only a wedge of about 30 degrees opening angle. Thus the point-spread function (PSF) from each petal is bow-tie shaped. Critical angle transmission (CAT) gratings<sup>11,12</sup> are mounted below the SPOs to disperse the light. The CAT gratings are arranged on the surface of a torus, and the CCDs that detect the diffracted light will be on the other side of the same torus. The gratings are blazed, so that light is dispersed preferentially to one direction. To minimize the distance between the ideal surface of the curved torus and the position of the flat gratings, the Rowland torus is slightly tilted.<sup>7,13</sup> Each petal has its own optical axes, but petals are arranged in pairs. As seen from the sky, one pair of petals disperses photons to the left, the other one to the right. This configuration

allows us to use just 16 CCDs arranged along a single circle to capture the zeroth orders of all channels and most of the dispersed signal. The CCDs are mounted in two cameras with eight CCDs each and about 40 cm of empty space between the cameras. A single point source will produce four dispersed spectra on the CCDs. Two of them will have the zeroth orders in the left camera and most of the dispersed signal in the right camera; for the other two channels the opposite is true. With the correct positioning of the Rowland tori, all four spectra will have their spectroscopic focus positions on the detectors to maximize the resolving power.

There are two important changes compared with reference 7: We originally envisioned that the two channels in each pair share an optical axis, so that we get only two traces on the detector. However, this requires a precise alignment of the plates holding the SPOs and gratings for those two channels with respect to each other. If instead each channel produces its own spectral trace, this alignment is much looser. The CCDs are wide enough in cross-dispersion direction that the signal will not overlap. The second change is the positioning of the CAT gratings under the SPOs. In reference 7 we just placed the gratings on a regular grid. Instead, we now use the exact positions from the engineering model. Four or six CAT gratings are positioned under each SPO; the layout for a single channel is shown in figure 2.

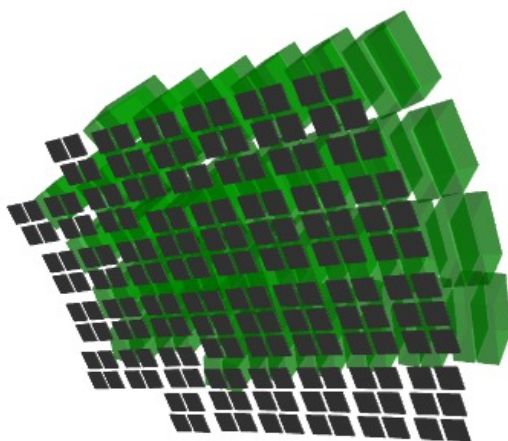


Figure 2. Shown are Arcus SPOs (green) and CAT gratings (gray) for a single channel. The layout of the other channels is symmetric to this one.

### 3. RAY-TRACING SETUP

Ray-trace simulations require input data on the reflection efficiency of the mirrors, the grating efficiency for different energies and blaze angles, the transmission coefficient of any filters, and the quantum efficiency of the CCDs as a function of wavelength. Those data can be calculated from tabulated properties of the materials,<sup>14</sup> or be supplied by vendors and the developers of parts. For Arcus, all these data is collected in a standard format in a versioned database and all Arcus ray-trace simulations draw from the same database, so that consistent input data is used when data from the same database commit is applied.

We use two independently developed ray-trace codes for Arcus and cross-check results between them as a way to test the reliability of the ray-trace codes. Both codes use slightly different approaches to parameterize the SPOs and thus results differ slightly. This difference is the largest in the predicted effective areas where it reaches up to 20% for a narrow wavelength region. For most wavelengths, the effective area agrees to about 10%. This number can thus be taken as an estimate for the “uncertainty” associated with the predicted effective areas.

Unless otherwise noted, the results presented in this article are derived with MARXS,<sup>15,16</sup> a Python-based ray-trace code that is available under an open-source license at <https://github.com/chandra-marx/marxs>. Arcus specific models can be found at <https://github.com/hamogu/arcus>. The MARXS code is tested with hundreds of unit tests and also verified by comparison to laboratory data and Chandra observations. See reference 7 for further details of the setup.

## 4. RESULTS

In this section, we show ray-trace results for Arcus that help to select the right parameters for the Rowland torus (radius, tilt angle) in section 4.1, the detector position (section 4.2), and the alignment budget (section 4.3). With these parameters, we can then numerically verify that the detector is at the best focus (section 4.4) and calculate resolving power and effective area in section 4.5.

### 4.1 Parameters of the Rowland torus

There are several pieces of information that constrain the choice of parameters for the Rowland torus, most importantly engineering constraints that limit the area available to place the SPO channels in the focal plane. Moving the channels too close together will lead to overlapping mounting structures, moving them too far apart requires a larger spacecraft boom. Our ray-traces explore a reasonable parameter space in the following parameters: channel spacing, blaze angle and radius of Rowland Torus.

We can write the equation of a torus that is not tilted as

$$\begin{pmatrix} x \\ y \\ z \end{pmatrix} = \begin{pmatrix} (R + r \cos \theta) \cos \varphi \\ r \sin \theta \\ (R + r \cos \theta) \sin \varphi \end{pmatrix} \quad (1)$$

. When we talk about the “Rowland circle”, we means the point that fulfill equation 1 with  $\theta = 0$ , which gives us a circle in the  $(x,z)$  plane. This equation can be generalized to tori where the center  $\vec{c}$  does not coincide with the origin of the coordinate system and the axis of symmetry is not parallel to one of the axes of the coordinate system. The axis of symmetry is given by a unit vector  $\vec{e}_y$ . We define a vector  $\vec{e}_R(\varphi) = \vec{e}_x \cos \varphi + \vec{e}_z \sin \varphi$  and can now write a generalized torus equation for points  $\vec{p}$ :

$$\vec{p}(\varphi, \theta) = \vec{c} + R \vec{e}_R(\varphi) + r (\vec{e}_y \sin \theta + \vec{e}_R(\varphi) \cos \theta) \quad (2)$$

. For a torus that is translated and rotated with respect to the coordinate system, we only need to rotate the  $\vec{e}_x$ ,  $\vec{e}_y$ , and  $\vec{e}_z$  and specify  $\vec{c}$ . For different blaze angles, we need to tilt the torus differently, leading to different  $\vec{e}_x$ ,  $\vec{e}_y$ , and  $\vec{e}_z$  and different  $\vec{c}$ . Each of the four channels lies of a different torus.

The remaining parameter is the distance between an on-axis grating and the focal point. For simplicity, we perform the simulations with a fixed value of 11800 mm. This will place the actual Arcus gratings (which are not located on-axis) a little more than 200 mm from the nodal plane of the mirrors. The exact location is chosen later based on the engineering of the SPO petals and the CAT grating petals. The other parameters are insensitive to variations of the Rowland torus radius of a few cm and do not need to be adjusted again. The calculations of the effective area assume two continuous strips of CCDs. In reality, there will be 2 mm gaps between the CCDs, leading to drops in the effective area. This can be somewhat mitigated by shifting one of the two CCDs strips by 3-5 mm compared to the position simulated here. This will have a very small impact on the effective area, but it avoids the problem that an important wavelength might fall into a chip gap in all channels at the same time. Also, we employ a cylindrical detector that follows the Rowland circle exactly. The real Arcus detector will consist of flat CCDs that are tiled and deviate slightly from the Rowland circle. These details are added in the next section.

We run a grid of models for a range of channel spacings, but from an engineering point of view a small distance between channels is strongly preferred because it allows the use of a smaller boom. After some initial exploration we found that we can match the mission baseline requirements with a channel spacing of 600 mm (measured center-to-center).

The most challenging science requirements for Arcus are the effective area and resolving power in the range of the O VII triplet (21.6-28 Å, accounting for a range of redshifts) and the C VI line (33.7-40 Å accounting for a range of redshifts). Different strategies can be used to optimize the placement of the detector. In the following, we show “maximize average  $A_{\text{eff}}$ ”, “maximize  $A_{\text{eff}}$  around O VII” and “maximize  $A_{\text{eff}}$  around C VI”. Figure 3 shows the results of one such simulation. The leftmost panel shows the detector position (measured as an angle

from the symmetry plane of Arcus and folded to positive values) of each detected photon. In this particular example, the zeroth order is located at  $\phi = 0.05$  (see large blue bar for zero order photons in the figure). The dispersed photons cover a range of angles larger than what can be covered by the given number of CCDs, so choices have to be made which photons are more valuable. The middle left panel in the plot shows  $A_{\text{eff}}$  for two different detector placement strategies.

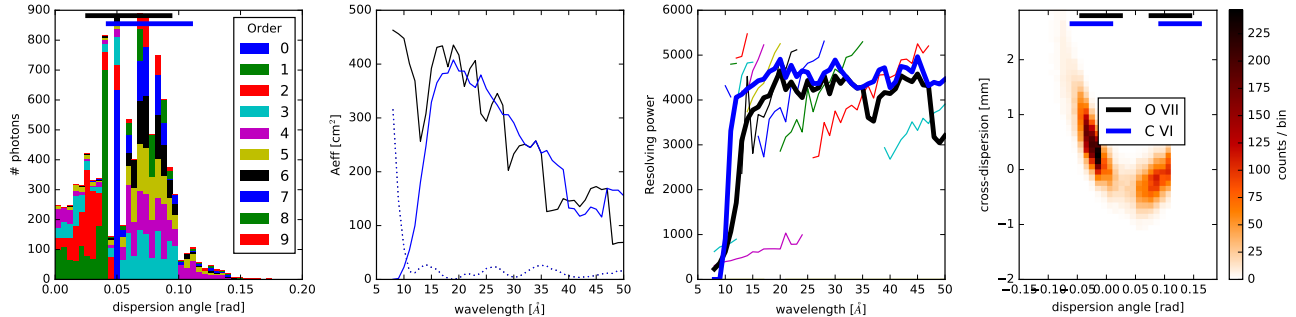


Figure 3. Simulation for blaze angle of  $1.8^\circ$ , radius of Rowland circle 5948 mm, radius of Rowland torus 5900 mm. The detector placement has been optimized for the effective area in O VII (black top line in leftmost and rightmost panel shows detector placement, also see black line in the two center panels) or C VI (blue lines). *leftmost panel*: This is a histogram of the dispersion angle measured from the plane of symmetry. This diagram is useful to understand the detector placement. In this particular case, the zero-order photons are at  $\theta = 0.05$  radian. *middle left panel*: Effective area for the black and blue scenario. Solid line is for dispersed photons (all orders added up) and the dotted line is for the zeroth order. *middle right panel*: Resolving power. The thick lines show the averaged resolving power for all dispersed orders, weighted by the number of photons in them. The thin, colored lines are resolving powers for individual orders for the first case (black scenario). *rightmost panel*: Detector image for a single channel. Note that this is not to scale, the y-axis is enlarged. The distribution of photons has a banana shape. This is due to the Rowland geometry, which optimizes the focus in dispersion direction at the cost of artifacts in the cross-dispersion direction.

Figure 3 gives a lot of detail on one particular simulation, but most important for the science requirements are  $R$  and  $A_{\text{eff}}$  in the O VII and C VI regions. Figure 4 shows results for simulations with different blaze angles. Small blaze angles give a lower  $R$  because most of the dispersed signal is contained in low orders not far from the zeroth order. On the other hand, low blaze angles lead to narrow blaze peaks so that the CCDs can catch most of the photons and thus a large  $A_{\text{eff}}$  is possible. Contrary, large blaze angles give higher  $R$  but smaller  $A_{\text{eff}}$ . For Arcus, a blaze angle of  $1.8^\circ$  is chosen.

## 4.2 Detector position

We now run more detailed simulations for the exact parameters of the Rowland tori chosen Arcus (blaze angle:  $1.8^\circ$ , channel separation: 600 mm (measured center-to-center),  $R$ : 5915.51 mm,  $r$ : 5945.79 mm. See equation 1 for a definition of the torus and figure 1 for the relative placement of channels.) placing flat CCDs with the appropriate gaps between them.

Figure 5 shows the simulated effective area curve zoomed in on the science requirement region O VII. For most of the wavelength range, the effective area is dominated by one spectral order, but a few more are seen with a significant number of counts. If an order falls into a chip gap for a specific wavelength, the number of counts in this wavelength drops to zero. However, photons are detected in the other orders so that the total effective area dips, but is still different from zero. Because the detectors are in slightly different positions in the left and right plot, different wavelengths fall into the chip gaps. In the right plot, the CCDs are positioned at larger distance from the zeroth order and thus the order 6 is seen out to  $> 23 \text{ \AA}$ , while on the left plot, essentially no 6 order photon is seen. On the other hand, order 3 is off the chip for the right plot for  $< 23.5 \text{ \AA}$ , while it is always seen in the left plot. The CAT gratings disperse more light into order 6 than order 3, so gaining order 6 at the cost of losing order 3 increases the average effective area.

Figure 6 summarizes a grid of models with different detector positions. We use a step size of  $\Delta\phi = 0.0005$  rad, which is comparable to the width of the chip gap. Thus, we do not always have a simulation where the

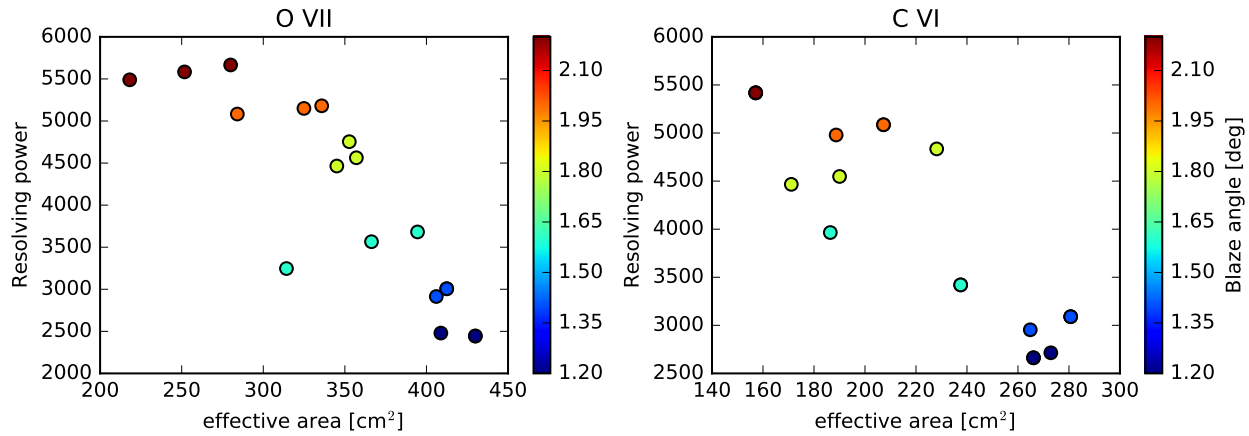


Figure 4.  $R$  vs  $A_{\text{eff}}$  for O VII and C VI for different blaze angles. All simulations have a torus radius of 5900 mm. The color of each dot shows the blaze angle in that particular simulation. There are three dots for each color, representing different strategies to position the CCDs (in some cases, only two dots are seen because results are so similar that dots overlap).

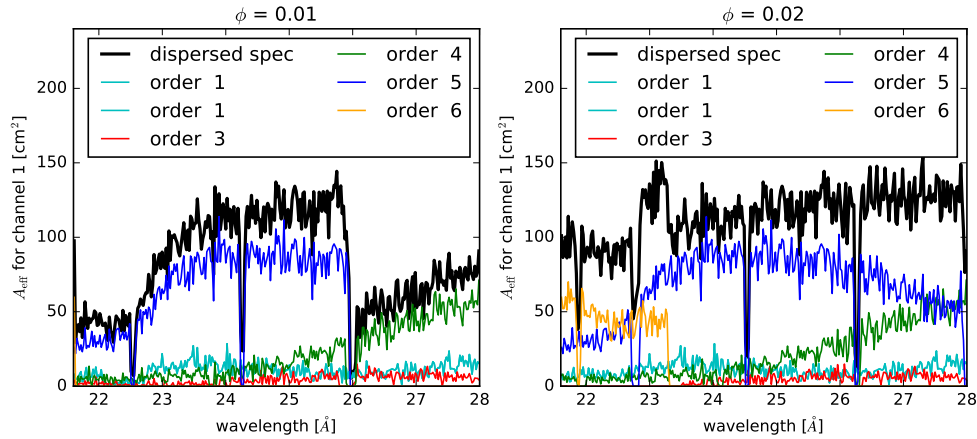


Figure 5. The black line shows the sum over all dispersed orders (including very low orders like order 1, where the spectral resolving power might be below the science requirements); the colors are for individual orders. The left and the right plot use the same input photons, but slightly different detector positions. In each plot, the position of the chip gaps can be clearly seen.

zeroth order is lost completely for every gap. For example, around 250 mm, the zeroth order is right on the edge of a CCD, leading to some loss of signal. Even if the black curve does not go to 0, these parameters need to be avoided to keep the zeroth order away from chip gaps even in the case of small mis-pointings. The requirement that each set of 8 CCDs must image two zeroth orders sets an upper limit for the inner edge of the innermost CCD at 300 mm, the location of the zeroth order.

Looking at the colored curves, we see that the behavior is relatively smooth. Because we average over a range of wavelengths, individual chip gaps are not important here. Somewhere in the range of wavelengths, there will always be a chip gap. Instead, the shape of these curves is driven by the overall shape of the blaze peak. For the blaze angle and focal length of Arcus, the blaze peak is wider than the area captured by just 8 CCDs on each side. That is why the placement shows so little sensitivity between about 150 and 300 mm. For every photon lost on the one side of the CCDs, we pick up another one on the other side. This makes the design of the cameras and the focal plane easier - optical constraints do not require an exact value for the position of the inner edge of

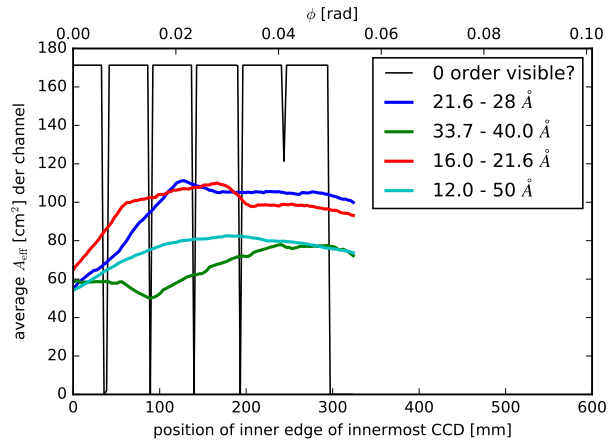


Figure 6. Average effective area in different spectral regions. The black line indicates if the zeroth order is detected on any CCD, it is just shown as yes (top) or no (bottom) and not scaled to the effective area of the zeroth order.

the innermost CCD, so this value can be found in trade-off between optics and engineering requirements.

### 4.3 Alignment Budget

The purpose of this section is to estimate the effect of alignment errors on the key performance characteristics of Arcus: Spectral resolving power and effective area. These numbers can then be used to guide the decision how to build up an error budget that specifies the allowable alignment tolerances for individual components. Naturally, there will be a trade-off: If one parameter is set looser, that will generally mean that all the other alignment tolerances have to be smaller. Science requirements put limits on the maximal allowable degradation of spectral resolving power and effective area and engineering constraints determine how well e.g. individual SPOs can be aligned into petals, how well the petals can be aligned to the forward assembly, and how well the forward assembly can be aligned to the detector housing. In general, tighter tolerances require more work, time, and money. We thus need to understand how important each possible degree of freedom is to the total performance of the system to identify those where significant work needs to go into the alignment. For some degrees of freedom in alignment only a ray-trace can really give the impact of misalignments, in other cases satisfactory estimates of the importance can be made analytically. Even in the second case, ray-trace calculations are a crucial cross-check.

The simulations here start from a perfectly aligned version of Arcus. Even this does not provide infinite resolving power, because this model already includes non-ideal effects that are not due to alignment, most notably, pointing jitter, which blurs the direction of the incoming photons, scatter on the SPO mirror surfaces, some astigmatism inherent in the design, and finite sizes of CAT gratings and CCD detectors, which means that they deviate from the ideal Rowland geometry. A ray-trace is run with this design and  $R$  and  $A_{\text{eff}}$  are calculated. After running the baseline version, one element of Arcus is shifted in one degree of freedom, e.g. all CCDs are shifted by 1 mm in the dispersion direction. The ray-trace is repeated, again  $R$  and  $A_{\text{eff}}$  are calculated, then all CCDs are shifted by 2 mm and so on. After testing out the parameters space in dispersion direction, the CCDs will be shifted in cross-dispersion direction. In this way, each element (for example the CCD array), will be “misaligned” by various amounts in one of 6 degrees of freedom (shift along  $x$ ,  $y$ ,  $z$ , and rotation around  $x$ ,  $y$ ,  $z$ ). In the first stage, only one degree of freedom is changed at a time, so there are no simulations where e.g. the CCD is misaligned in  $x$ ,  $y$ , and  $z$  simultaneously. This is purely a computational limitation. Simulations are done for about 30 steps for each degree of freedom, which requires about  $6 * 30 = 180$  simulations for the CCDs and similar numbers for SPOs, CAT gratings etc.. Together, the first exploration where only one degree of freedom is varied at a time is based on several thousand simulations. If we wanted to explore the full 6-dimensional parameter space, we would need  $30^6 \approx 10^9$  simulations for the CCDs alone.

For small tolerances it is not an unreasonable assumption that the misalignments in different degrees of freedom just add up and this can be used to build the total misalignment budget. In a second step, we can then run ray-traces where all degrees of freedom are varied according to the misalignment budget and thus check if the assumptions going into combining the misalignments in different degrees of freedom hold or if non-linear interactions degrade  $R$  and  $A_{\text{eff}}$  more than expected. To keep the computational load reasonable, we simulate only one channel of Arcus. Since spectra from each channel will be extracted separately and there is symmetry between the channels, most results apply equally to all channels.

### 4.3.1 Format of alignment plots

The next few subsections present ray-trace results where one degree of freedom for an alignment is changed compared to the perfectly aligned Arcus model. In most cases, six plots are presented. The top row shows translations, the bottom row shows rotations. The first plot in each row is the translation in (or rotation around) the global telescope x-axis, the second plot is for the y-axis, and the last one for the z-axis. The global Arcus coordinate system has the z-axis parallel to the optical axis, the x-axis is the grating dispersion direction and the y-axis is the cross-dispersion direction. Rotations are performed around the center of an element (e.g. the center of an SPO petal); this is described in detail for individual elements below.

Each figure shows the shift or rotation angle on the x-axis and then plots  $R$  with a solid line, the value can be seen on the left y-axis of the figure. Overplotted is the effective area with dotted lines, the value can be seen on the right y-axis of the plot. Note that these effective areas are for one channel only, so the total Arcus effective area will be four times larger. The exact numbers for the effective area are subject to change as we continue to develop the ray-trace simulation, for example, currently, the simulation does not include obscuration by a thin hexagonal support mesh under the optical blocking filter. However, most of the missing effects are just an overall factor and the relative change in  $A_{\text{eff}}$  with increased misalignment is very robust.

Ray-tracing is performed for three different representative wavelength in the Arcus bandpass, shown as different colored lines on the plots.

When looking at the figures below, the following points should be kept in mind:

- Each simulation is done with 200000 photons, so some scatter due to Poisson noise is inevitable. In some cases,  $R$  is essentially unchanged, so that the y-axis range in the plots is shown from e.g. 4600 to 4800. While the lines on the plot zig-zag between the top and the bottom, the real change in  $R$  is only a few percent, entirely consistent with Poisson statistics.
- $A_{\text{eff}}$  is given summed over all dispersed orders that fall on a CCD and  $R$  is the average resolving power, where the resolving power from individual orders is averaged weighted by the number of photons in that particular order. Thus, it is possible, that  $R$  in the plot increases with increasing misalignment if  $A_{\text{eff}}$  drops at the same time. This happens when an order with lower-than-average  $R$  drops off the CCD (thus reducing the summed  $A_{\text{eff}}$  and increasing the average  $R$ ).
- Note that the zoom level for all axes (bottom, left, right) is chosen differently for each plot to highlight relevant features.

In the following sections, there are two different ways to apply misalignments. In the first case, we apply a deterministic change to all elements at once, e.g. we shift the entire SPO petal by 5 mm to the left. In this frame, a global rotation would mean that the entire SPO petal is rotated rigidly by some angle, so that the SPOs in the center move very little, while the SPOs on the outside rotate with a larger lever arm. These calculations are done for a range of negative and positive values and are shown with a grey background. In the second case, we apply misalignments to each element individually. For example, we move the SPOs within the (stationary) SPO petal. In this case, the actual change for each SPO is drawn from a Gaussian distribution centered on 0 and with a Gaussian  $\sigma$  corresponding to e.g. 5 mm. The average misalignment of all SPOs will be close to 0 in this case, but they are all shifted relative to each other. These simulations are shown with light pink background.

In addition, there are a few plots with light blue background. These look at a loss of  $R$  and  $A_{\text{eff}}$  from changing Arcus design parameters which are not alignment tolerances but do contribute to the width of the observed line-spread function. While the default for all alignment tolerances is 0 (and their values are only different from 0 in the section explicitly discussing their contribution), the pointing jitter and the scatter from the SPOs have non-zero default values. Both SPOs and star tracking system are not build by the Arcus team, but are supplied by other vendors. If all of these numbers were set to 0, Arcus in the simulations would reach very high values for  $R$ . As a consequence, even very minor misalignments in any axis would cause a significant (relative) drop in  $R$ , when in practice the alignment requirements are much more relaxed because of the width of the line spread function that is already introduced by the scatter from the SPOs and the spacecraft jitter.

### 4.3.2 Pointing jitter

Pointing jitter is not technically an alignment tolerance, but it affects the optical performance of Arcus in much the same way as misalignments between the optical components and it thus makes sense to treat it here. In this context, the “jitter” that matters is the uncertainty in the aspect solution, or, in other words, the difference between the true pointing direction and the tabulated pointing direction at the time of photon arrival. There are several reasons why the true pointing direction at the time of photon arrival might be unknown. They fall in two groups: First, the photon arrival time is only known within a certain time interval (the frame time). If the spacecraft moves between the beginning and the end of a frame, we cannot know where exactly it pointed when the photon arrived even if the spacecraft pointing was known perfectly all the time. To reduce this uncertainty, the spacecraft has to move slowly. Second, there are uncertainties to the instantaneous true pointing direction itself from e.g. fitting uncertainties for determining the centroids of the stars observed with the star tracker.

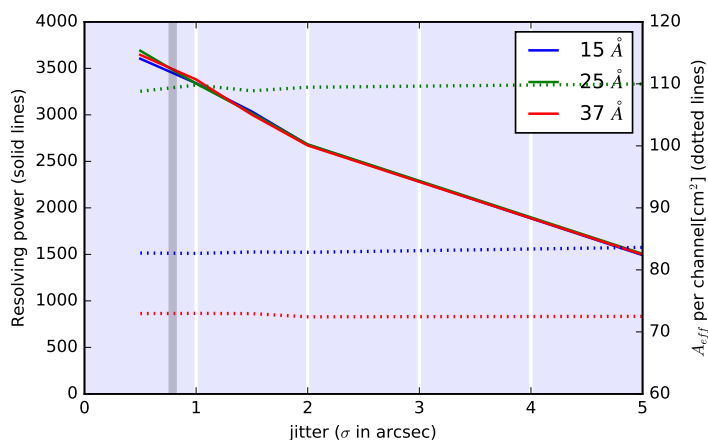


Figure 7. Change of  $R$  and  $A_{\text{eff}}$  with changing spacecraft jitter. See text in section 4.3.1 for an explanation of the figure format. The gray bar marks the value for the jitter sigma that is used in all the misalignment simulations.

Figure 7 shows how uncorrected jitter can quickly reduce the spectral resolving power if the pointing is not controlled to within about 1 arcsec. The gray bar marks the value for the jitter sigma that is used in all the misalignment simulations.

### 4.3.3 Detectors / Misalignment between front and rear assembly

There are three main elements in Arcus: SPO petal, CAT grating petal, and camera. All that matters for the ray-trace is their relative position. Here, we show simulations where the entire focal plane is shifted or rotated. The center of rotation is the point between the two CCD arrays. This can happen if the camera is mounted with some misalignment in the rear assembly or equivalently, this can represent a misalignment between front and rear assembly, e.g. a twist in the boom. Thus, “shift along z” (top right plot) is a change in focus.

We discuss the top row in figure 8 in order of importance, which is right to left: The plots show that the most important degree of freedom is a change in focus. A shift along y is irrelevant, as long as it is small enough to

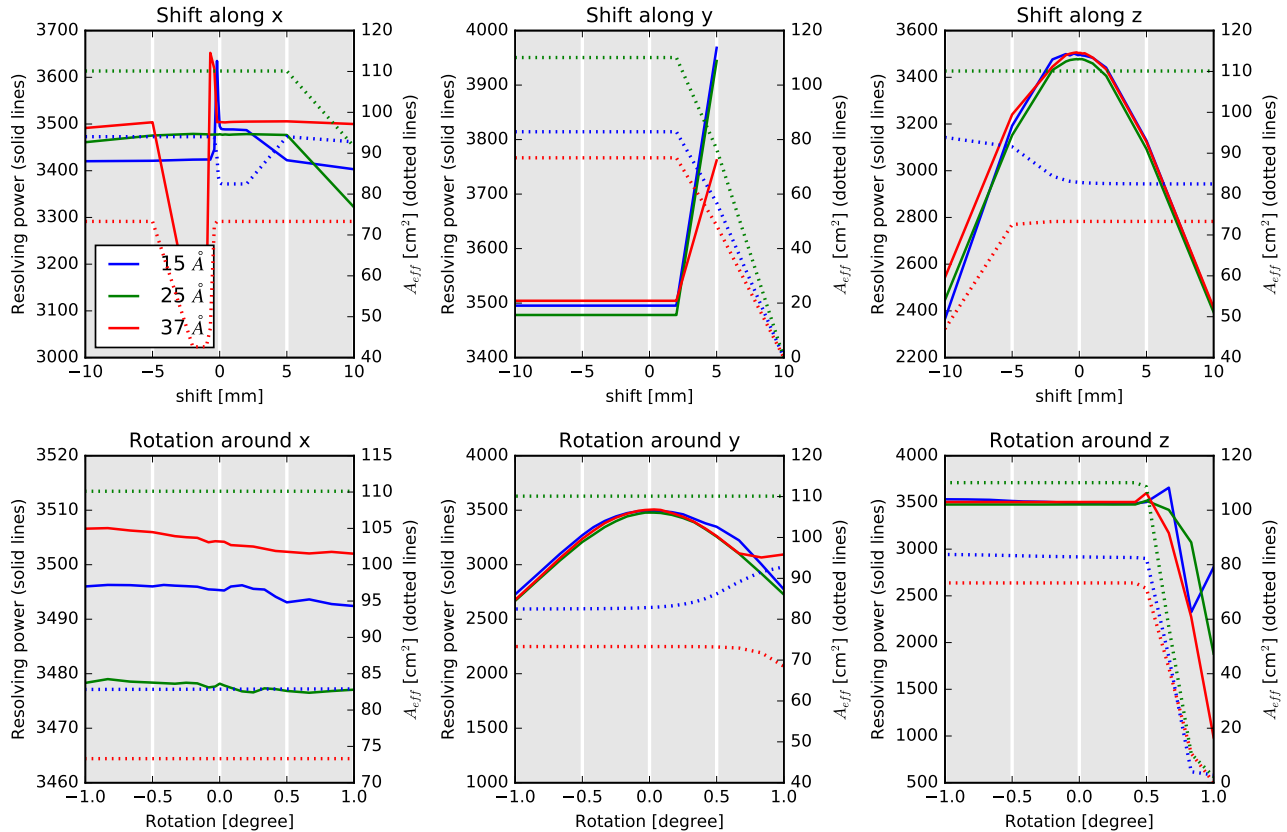


Figure 8. Change of  $R$  and  $A_{\text{eff}}$  with detector misalignment. See text in section 4.3.1 for an explanation of the figure format.

keep the dispersed spectrum on the CCDs. For the particular channel simulated here that happens for  $y$  shifts for about  $-15$  mm on one side and about  $+5$  mm on the other side. A shift of  $5$  mm or more will drop at least one channel of the detector but in practice, this could be compensated by using offset pointing (placing the science target not on, but shifted with respect to the optical axis).

The curves for changing  $R$  with shift in  $x$  (top left) show some spikes when an order hits a chip gap. For example, two orders contribute to the signal in the red curve. At  $-2$  mm one of them hits a chip gap, causing a sudden drop in  $A_{\text{eff}}$  and also in  $R$  ( $R$  is averaged over all contributing orders, but only one order which happens to have a lower  $R$  is detected at this position). Note that chip gaps are inevitable. There will always be some wavelength in a chip gap. At  $0$  mm it might be  $35\text{\AA}$ , at  $-1$  mm it is  $36\text{\AA}$ , and at  $-2$  mm it is  $37\text{\AA}$ . The overall performance of the instrument averaged over a range of wavelengths is unaffected by this. Shift along  $x$  matters in principle because the focal plane is curved. If the CCDs move in the dispersion direction, the spectrum will be slightly out of focus but the plot shows that shifts up to a few mm have little impact. This opens an additional possibility to mitigate the effect of chip gaps. In the current design, we have two sets of  $8$  CCDs, which are symmetrical with respect to the mid-plane of Arcus except for a small shift of a few mm, which means that the two channels from one pair of petals will have other chip gaps than the channels from the other pair of petals. In this configuration each pair of channels will have the chip gaps at the same wavelength. Based on the simulation here, we can additionally introduce a small offset, say  $4$  mm, in  $x$ -direction between the two channels of the same petal pair. That way, no two spectra will have chip gaps at that same position.

The bottom row in figure 8 shows the same phenomena as the top row. Rotation around the dispersion direction has little effect on  $R$ , rotation around  $z$  is only relevant once it becomes so large that the signal drops off the CCDs (about half a degree). Rotation around  $y$  (the cross-dispersion direction) is essentially the same as

a defocus. This rotation makes the CCDs move up or down on a lever arm, causing the photons be the imaged at the wrong z position.

#### 4.3.4 CAT gratings

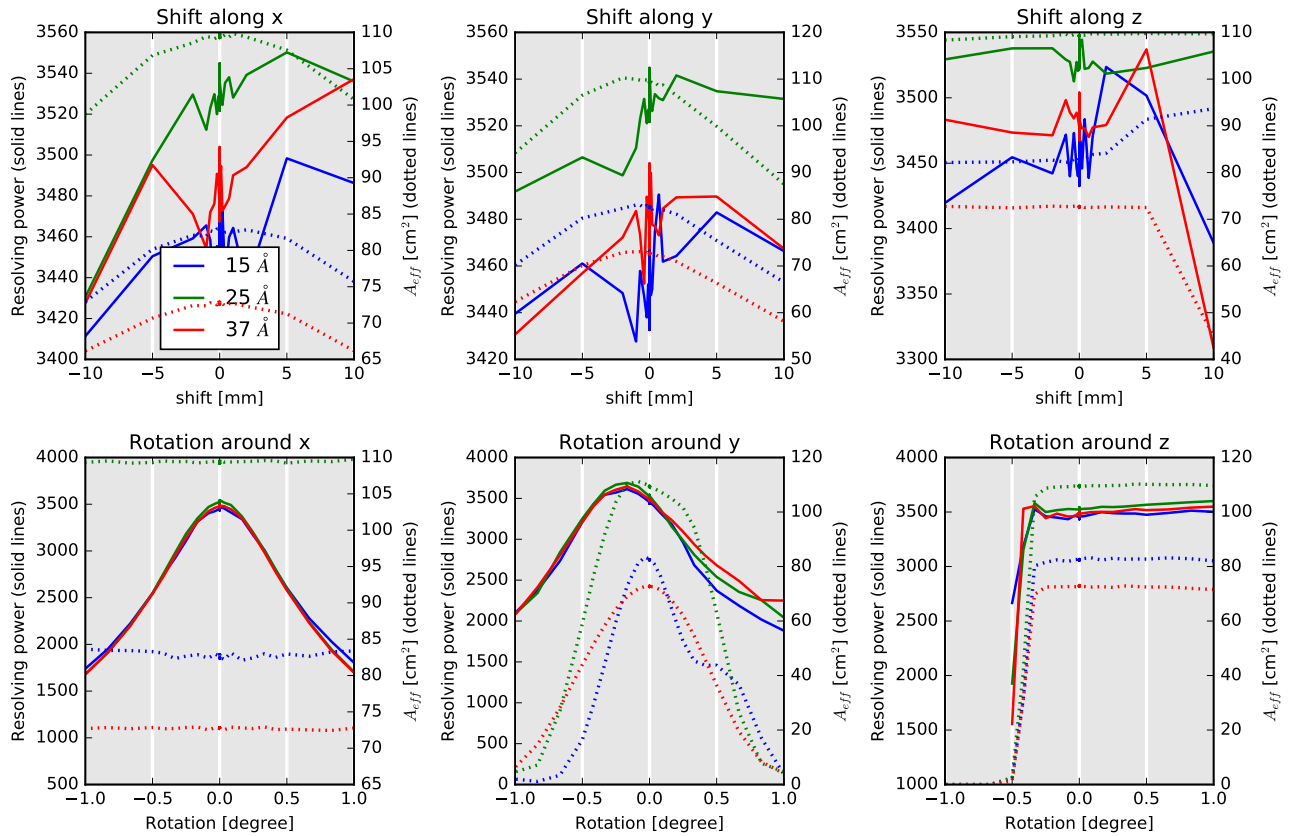


Figure 9. Change of  $R$  and  $A_{\text{eff}}$  CAT grating petal misalignment. See text in section 4.3.1 for an explanation of the figure format.

Figure 9 shows a change in the CAT grating petal position, while the SPO petal and the cameras are fixed. The petal is very robust to translations in any axis. Shifts in  $x$  and  $y$  move the petal almost tangential to the Rowland torus and thus changes of even a cm or two have little effect on  $R$ ,  $A_{\text{eff}}$  only decreases because the gratings are carefully aligned under the petals and shifting leads to more shadows falling on the active area of the CAT gratings. A translation along the optical axis is essentially equivalent to choosing a Rowland torus with a slightly smaller radius and that has little impact that long as the shift is small compared to the radius of the torus (6 m). The misalignment steps are chosen to densely sample the parameter space close to 0 and fewer simulations are done at larger shifts. In these plots, that are dominated by the Poisson scatter of the Monte-Carlo simulations, the lines look thus jittery close to 0, where many datapoints are located.

Rotations are calculated around the center of the CAT grating petal. Rotations around either  $x$  and  $y$  mean that the CAT gratings on one side move up, while the other side moves down changing the path length of the diffracted photons. Those photons coming from the high CAT gratings travel further along the dispersion direction than those from the low gratings, thus causing the dispersed spot to smear out, which reduces  $R$ . Rotation around  $z$  changes the direction of the dispersed light and for large angles, the dispersed orders miss the CCD.

Figure 10 shows misalignments of windows (a window is a group of four or six CAT gratings under one SPO mirror module, see figure 2) within the CAT grating petal, while all the individual CAT gratings are at their

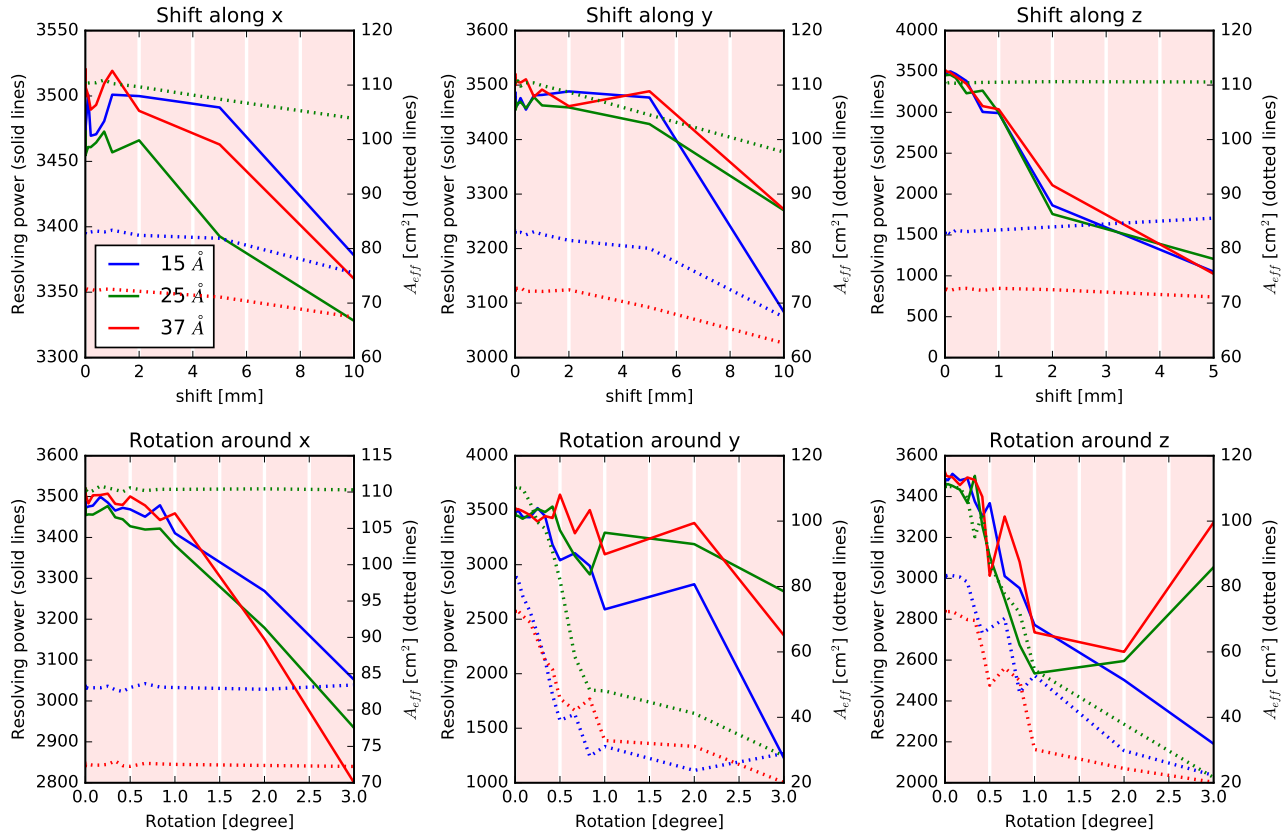


Figure 10. Change of  $R$  and  $A_{\text{eff}}$  for misaligning CAT grating windows (groups of four or six CAT gratings). See text in section 4.3.1 for an explanation of the figure format.

nominal positions with respect to the window center. Note that the plots for shift in  $x$  and  $y$  contain some unphysical space. For shifts larger than a few mm windows would overlap. In practice the window frames will prevent that, but in the simulation some photons go through two CAT gratings. Note that a shift along  $z$  (the optical axis) of even 1 mm reduced  $R$  significantly here, while a shift of the entire petal by the same amount has little impact. If only a few CAT gratings are shifted up or down, then the photons which are diffracted earlier (closer to the SPOs) are traveling a longer path and make it further along the dispersion direction than photons diffracted at the nominal position, thus smearing out the orders and reducing  $R$ .

Rotations around  $x$  and  $y$  have little effect on  $R$  for angles below a degree. Since the facets have a finite size, their edges differ from the Rowland torus by a little already, and adding a little more rotation does not change much. Rotations in  $y$  quickly reduce  $A_{\text{eff}}$  though, because the CCDs are placed for a certain blaze peak. Rotating the CAT gratings shifts the blaze peak and photons to orders that miss the CCDs. Rotation around  $z$  causes more and more signal to miss the detector. Unlike in the previous plot, there is no sharp cut-off because the grating windows in the simulation have a distribution of rotation angles, and the larger the Gaussian  $\sigma$  is, the more CAT gratings will send their dispersed photons to positions where they cannot be detected.

Figure 11 shows misalignment of CAT gratings with respect to the windows they are mounted to. It is very similar figure 10, which shows misalignments of the windows with respect to the grating channel. What matters for the direction that a photons has after dispersion is the position and orientation of the CAT grating relative to the SPO. It is irrelevant if an misalignment is caused by the tolerance between CAT petal and window or between window and individual grating. The only difference is in rotations. In figure 11, rotations are applied around the center of a CAT grating, while in figure 10, rotations are applied around the center of a window. Since windows are larger (they contain four or six CAT gratings), a rotation around the window center will move

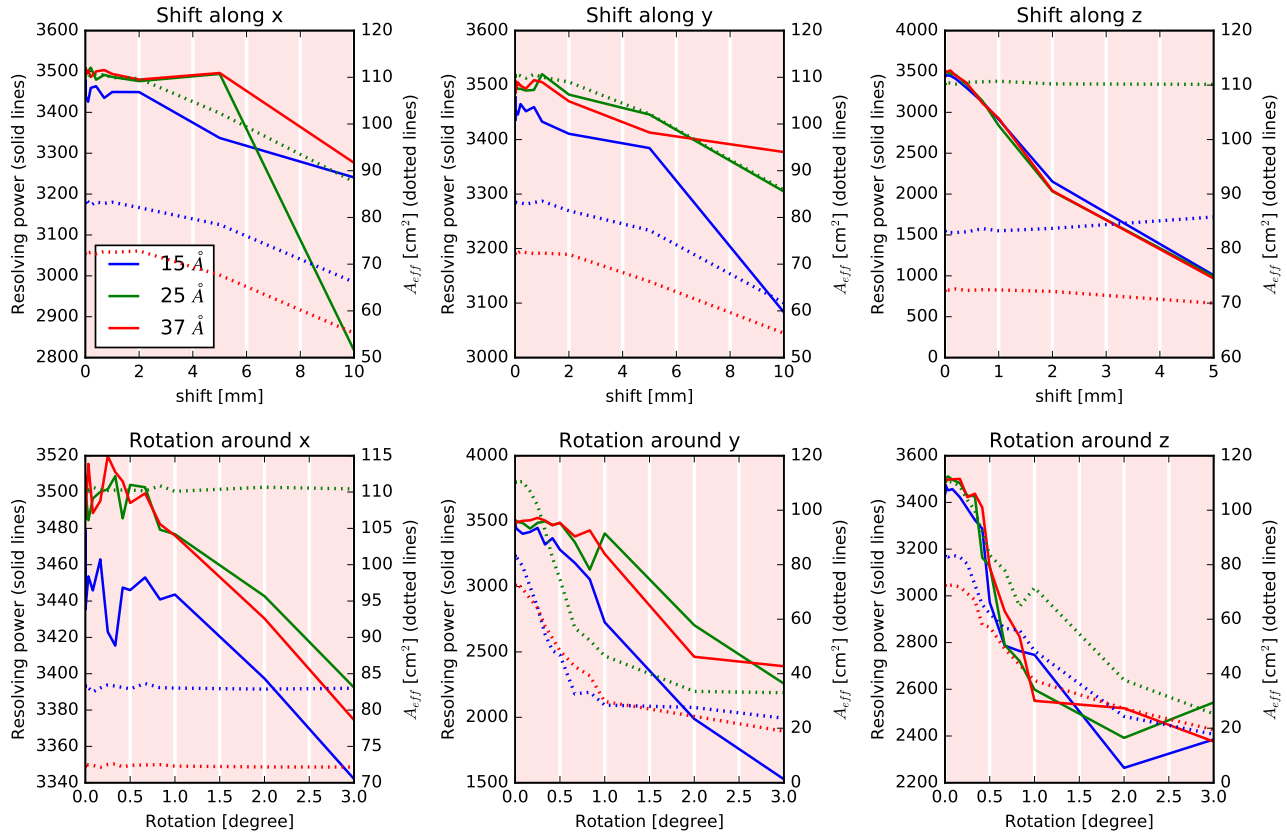


Figure 11. Change of  $R$  and  $A_{\text{eff}}$  for misaligning individual CAT gratings. See text in section 4.3.1 for an explanation of the figure format.

the edges of the CAT gratings more than a rotation around the center of each CAT gratings.

#### 4.3.5 SPOs

The SPO model used in MARXS raytracing is fairly simple (just a perfect mirror with additional in-plane and out-of-plane scatter) but it works well for on-axis sources and small angles. For large angles (many arcminutes) vignetting becomes important and the size of the PSF increases. Both effects are not included in these simulations. However, the results for translations should be robust and the results for rotations should be good for small angles.

We refrain from showing figures for these simulations due to the limited space in this proceeding.

#### 4.3.6 Scatter in the SPOs

Last, we examine the importance of the scatter in the SPOs in figure 12. This scatter comes from surface figure errors or particulates on the SPO surface. Our ray-trace simulation does not model the shape of an SPO in 3D, instead, it uses a simplified model that treats each SPO module as a thin lens with perfect imaging quality. It then adds scatter in the plane of reflection (mostly broadening the photon distribution in the cross-dispersion direction in our design) and out of the plane of reflection (mostly influencing the photon distribution in dispersion direction). The magnitude of this scatter is matched to observed quantities for SPOs that have been manufactured and measured in the laboratory.<sup>10, 17</sup> For each photon, in plane and out of plane scatter is drawn from a Gaussian distribution with a given  $\sigma$ . In figure 12 the out of plane scatter was set to 0 for the simulations shown in the left plot, and the in plane scatter was set to 0 for the simulations shown in the right plot. For perfect mirrors, the maximum  $R$  is about 10000; this number is limited by the pointing jitter that is

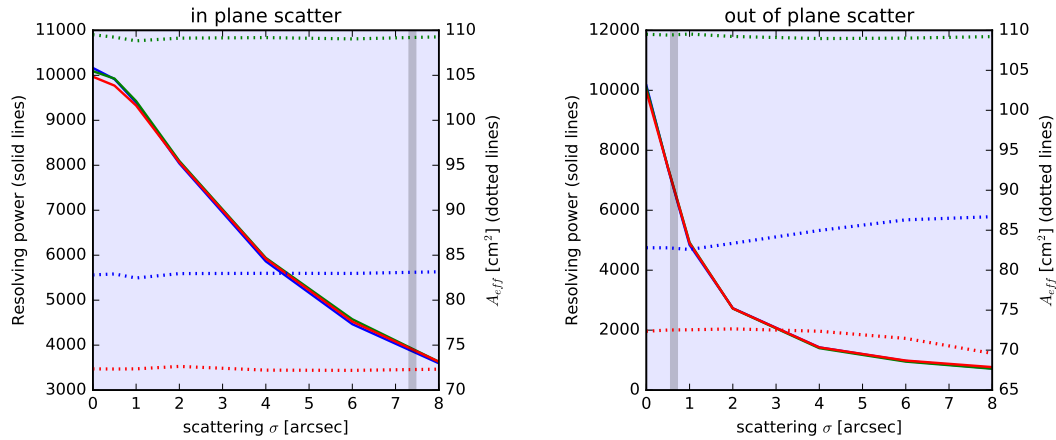


Figure 12. Change of  $R$  and  $A_{\text{eff}}$  for different values of the mirror scattering function, i.e. different PSF sizes. See text in section 4.3.1 for an explanation of the figure format.

alignment unit	trans x mm	trans y mm	trans z mm	rot x "	rot y "	rot z "
individual SPO in petal	0.004	0.033	0.017	100	100	3
SPO petal to front assembly	0.000	0.000	0.000	0	0	0
CAT petal to SPO petal	0.333	0.333	0.333	100	100	200
CAT windows to CAT petal	0.333	0.333	0.067	100	60	100
individual CAT to window	0.333	0.333	0.067	100	60	100
Camera to front assembly	1.667	0.667	0.333	60	60	60

Table 1. Arcus alignment budget ( $1\sigma$  values). Note that there is no error given for the alignment of the SPO petal to the front assembly because the position of the SPO petal is defined to be the base orientation. The CAT grating petal and the camera in the rear assembly are measured with respect to the SPO petal position.

included in these simulations (see above) and also by the finite size of the grating facets, which deviate from the ideal mathematical Rowland torus.

Gray bars in each plot mark the fiducial  $\sigma$  for the scatter that is included in all the other simulations shown in this article. From the left plot, we can see that  $R$  for Arcus in general is limited by the size of the in plane scatter and any improvement of this quantity will also improve the overall  $R$ , at least until other effects and misalignments become dominant.

(Note that instead of a Gaussian  $\sigma$ , the full width at half maximum (FWHM) of the Point-spread-function (PSF) or half-energy width (HEW) is often quoted.)

#### 4.3.7 Alignment budget

In this step, all possible alignment tolerances are varied at the same time according to the alignment budget in table 1, where the numbers in the budget are decided as a trade-off between engineering requirements, cost, and the acceptable loss of  $R$  and effective area. The alignment budget assumes that all alignment tolerances contribute independently and the simulations here are designed to check this assumption. Some misalignments might cancel out in practice, others might have a multiplicative effect. Full ray-tracing is the best way to check that and to predict final instrument performance. There are two sources of uncertainty in predicting how much  $R$  and  $A_{\text{eff}}$  change compared to the baseline for a set of alignment tolerances. First, ray-tracing is a Monte-Carlo simulation with a finite number of rays. It is thus possible, that the signal in one run is narrower than in the baseline scenario just by chance. Second, misalignments are statistical. For each element they are drawn from a Gaussian distribution. Thus, the predicted  $R$  and  $A_{\text{eff}}$  vary from simulation to simulation. Figure 13 shows how  $R$  and  $A_{\text{eff}}$  change for the baseline alignment tolerances for three wavelengths. On average,  $R$  is reduced by about 2% relative to the baseline; indicating that the alignment budget is unlikely to degrade the performance

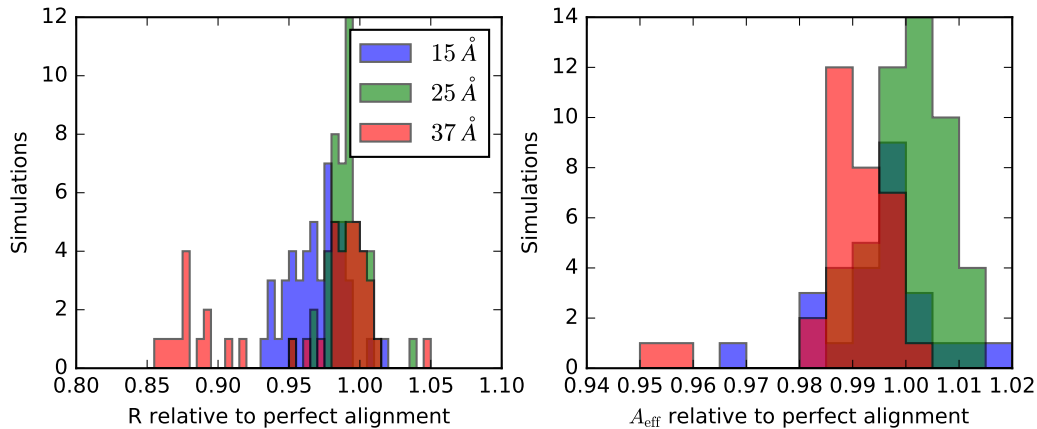


Figure 13.  $R$  and  $A_{\text{eff}}$  relative to a perfectly aligned Arcus for different realizations of the misalignment budget in table 1.

significantly. However, there is a finite probability to lose more than 10% of  $R$  for unlucky scenarios.  $A_{\text{eff}}$  stays essentially unchanged in all simulations.

Differences are visible between the different wavelengths. At 37 Å two dispersed orders (order 3 and 4) contribute, but order 3 is close to the edge of a CCD and order 4 is close to a chip gap. If either one is lost,  $R$  or  $A_{\text{eff}}$  will suffer. In contrast, the signal at 25 Å is dominated by order 6, comfortably in the middle of a CCD. Thus, the two plots above should not be interpreted as “longer wavelength will suffer more”; crucial orders are close to a chip gap in different spots over the Arcus bandpass. Instead, the plots should be read as showing the range of effects that the baseline misalignment can have on  $R$  and  $A_{\text{eff}}$ .

#### 4.4 Numerical focus verification

Here, we want to test that the analytically derived detector position is indeed correct. From theory, we know that the detectors should be placed tangential to the Rowland circle and Arcus follows this layout. Here, we want derive the ideal detector position numerically to confirm that the Rowland geometry is in fact valid; one might think that non-ideal effects such as the finite size of the flat facets might lead to a slightly distorted focal surface.

After passing the CAT gratings, the rays are distributed both in dispersion and in cross-dispersion direction. Travelling down in the direction of the focal plane, the beam becomes narrower in both directions. Eventually, it reaches a point where it is the narrowest in dispersion direction, but still relatively wide in cross-dispersion direction (this is the “spectroscopic focus”), the PSF is elongated. Beyond this point, the beam widens again in dispersion direction, but continues to narrow in cross-dispersion direction, the PSF becomes rounder until it reaches (approximately) a circle (“imaging focus”). This is the point where the total PSF size is smallest. The beam continues to narrow in cross-dispersion direction, and widen in dispersion direction until it passes the minimum in cross-dispersion direction (“cross-dispersion focus”), the PSF is elongated again, but with the long axis in dispersion direction now. Beyond that, the beam get wider in both directions again.

We take a grid of simulations for different wavelength points and iterate over all optical channels and all orders which happen to have  $> 20$  rays in that channel and order for that specific wavelength. In total, that gives us  $> 2000$  sets of rays for which we can numerically find the spectroscopic focus, the imaging focus and the cross-dispersion focus.

Figure 14 zooms in on one camera with eight CCDs. Looking this closely, one can see that the CCDs match the position of the numerically determined focus values better than 1 mm, which is the acceptable distance from the ideal focus before defocussing degrades the spectral resolving power significantly. A fit by-eye indicates that the numerically determined focus is about 0.2 mm below the CCD position. This deviation is more than expected from the scatter. This difference is smaller than the focus tolerance determined from our tolerancing

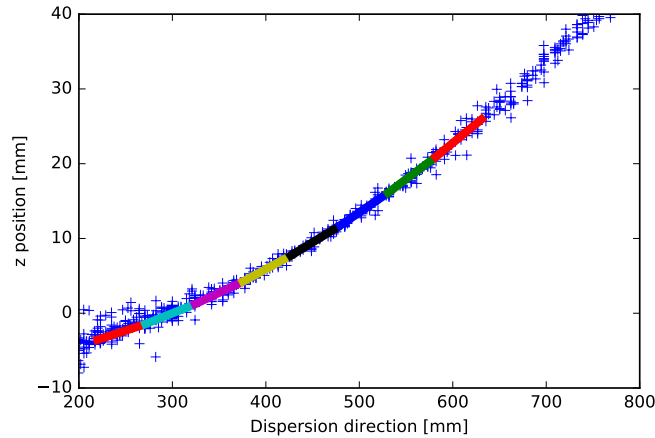


Figure 14. The plot below shows the position of best focus determined for all wavelengths, channels and orders. Together, these points map out the focus surface well. Overplotted are the Arcus CCD positions with colored lines.

study. More investigation can be done later, but a likely cause of the 0.2 mm distance is the finite size of the CAT grating facets. In Arcus, we place the center point of a CAT grating on the Rowland torus and then apply the correct rotation and blaze angle. While the CAT grating center will always be exactly on the Rowland torus, the edges will typically be located a little “above” the Rowland torus. This means that, on average, the rays get diffracted at a slightly larger distance from the focal point than they should be. This is equivalent to using a slightly larger radius for the Rowland circle, and a slightly larger radius means that the CCDs need to be placed a little further away from the CAT gratings, consistent with the numerical best focus being about 0.2 mm lower than the CCDs on the Rowland circle.

#### 4.5 Resolving power and effective area

In the previous sections, simulations are done for just a few wavelength points and  $R$  and  $A_{\text{eff}}$  are calculated for those specific wavelengths. In this section we present simulations on a much finer wavelength grid.

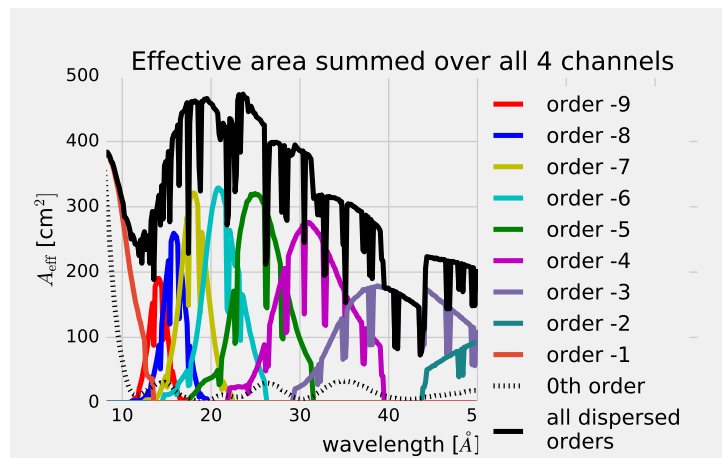


Figure 15. Effective area per diffraction order summed over all four channels.

Figure 15 shows the effective area curve for Arcus based on the instrument setup and nominal alignment for every element. The effective area for all four channels is summed. The contribution of individual grating orders is shown with colored curves. Each of the curves has a number of dips in it when an order falls into a chip gap.

For any individual channel, the effective area drops to 0 in this case, but the channels are placed such the the chip gaps do not coincide in all of them, so the summed effective area suffers, but some signal is still detected.

The black curve sums the effective area of all detected dispersed orders, irrespective of their spectral resolving power. However, for most of the wavelength range, only orders that are very similar in resolving power (e.g. orders 4 and 5 at 30Å contribute anyway. The only exception to this rule is the region around 12Å, where both order 1 and 9 contribute to the observed signal, with significantly different  $R$ .

We define the resolving power as:  $R = \frac{\lambda}{\Delta\lambda} = \frac{d_x}{FWHM}$  where  $\lambda$  is the wavelength of a spectral line with negligible intrinsic width, and  $\Delta\lambda$  is the observed width of this feature. Since the detector does not give the wavelength directly,  $d_x$  and the  $FWHM$  are linear distances measured as follows: Events that hit a CCD are projected (not propagated, that would bring them out of focus) into a plane. The  $FWMH$  is the full width at half maximum of the event distribution and  $d_x$  is the distance between the center of a diffracted order and the zeroth order. Since the CCDs are flat and do not follow the Rowland circle exactly, the  $R$  is somewhat lower than the  $R$  expected on the Rowland circle. However, this effect is so small that it is negligible in practice. There is one problem with this procedure: If the center of the photon distribution is very close to a chip gap, then only a fraction of the true distribution is visible on the chip and naturally the  $FWHM$  of this distribution will be narrower than the true distribution. Thus, we also calculate the  $R$  for a cylindrical detector on the Rowland circle and use the  $R$  derived this way for positions close to the chip edge.

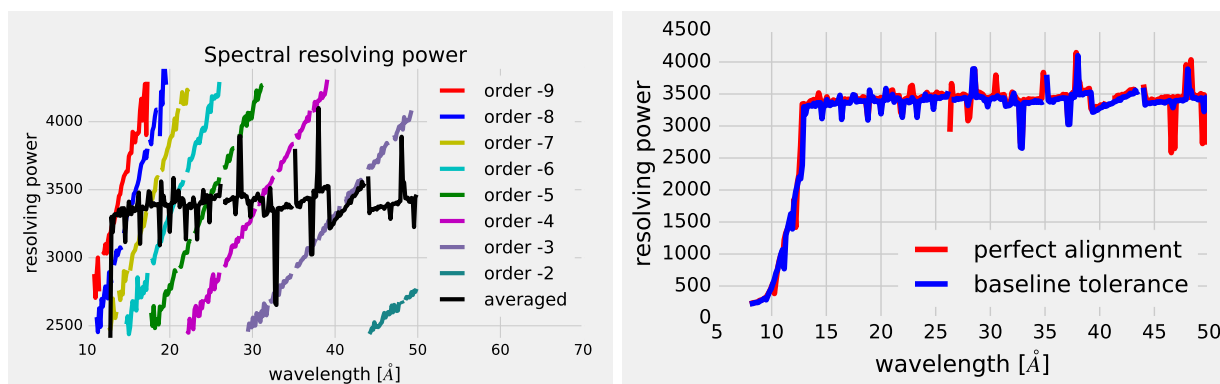


Figure 16. *left*: Spectral resolving power for individual orders. The resolving power is only calculated if a certain minimum number of photons is detected in an order. If most photons fall into a chip gap, then values on the curve might be missing. *right*: Resolving power averaged over all channels and all dispersed spectral orders. When averaging, values are weighted by their respective effective area.

Figure 16 (right) shows the resolving power averaged over all channels and all dispersed spectral orders. When averaging, values are weighted by their respective effective area. There are some drops in  $R$  that occur when a wavelength is observed where two orders with slightly different  $R$  contribute and one of them falls into a chip gap for a certain wavelength. In the region 39-44Å only a single order contributes, and  $R$  rises with wavelength as it does for each individual order.  $R$  in each order increases with wavelength because the order moves further away from the zeroth order for increasing wavelength (see figure 16, left) and thus  $d_x$  increases while  $FWHM$  changes little. For small wavelengths  $< 12\text{\AA}$  very low orders contribute to the signal, bringing down the average  $R$ . Figure 16 (right) shows almost no difference between the perfect alignment and the baseline alignment tolerance scenario. This is consistent with the results in section 4.3.7.

Over most of the wavelength range, the averaged  $R$  is almost constant. That is not a coincidence, but rooted in the physics of CAT gratings. The  $FWHM$  is dominated by the mirror point spread function (PSF). In practice the PSF is slightly energy dependent, but this is not captured in the simple mirror model used for these simulations. All other effects on the  $FWHM$  are very small (for example, it also depends on where on a CCD the signal falls since the CCDs are not curved and do not follow the Rowland circle exactly, but for Arcus this effect is negligible). So, the only variable left is  $d_x$  the distance of the spot from the zeroth order. Photons with a longer wavelength are dispersed to larger distances and thus have larger  $d_x$  which explains why  $R$  increases with

wavelength for every order. On the other hand, CAT gratings most efficiently diffract photons to a particular angle (the blaze peak). Thus, for longer and longer wavelengths the signal in an order becomes weaker, because the position of the order moves away from the blaze peak. At the same time, the next lower order moves towards the blaze peak and becomes increasingly stronger. In other words, the higher order (which has a higher  $R$ ) drops in effective area, while the next lower order gains effective area. Together, this means that the averaged resolving power stays essentially constant.

## 5. END-TO-END SIMULATIONS

In addition to the ray-traces described here, extensive end-to-end simulations are done with SIXTE. These simulations use the post-CAT grating distribution of rays simulated from the ray-traces described here. They fit this distribution and build a library of line-spread-functions which gives SIXTE the ability to interpolate the grid of raytraces for off-axis positions and arbitrary photon energy. In particular, SIXTE uses a much more detailed CCD model than MARXS and thus detector effects like pile-up and order sorting in the presence of limited energy resolution can be simulated there. The end-to-end simulations are described by Wilms et al. in this volume.

## 6. SUMMARY

Arcus is a proposed MIDEX mission for soft X-ray spectroscopy. It consists of four channels, each of which follows a Rowland torus design with a tilted torus. The tori are placed in space in such a way that the same CCD read-out array can be used for all four channels. Our ray-traces predict the Arcus performance for different parameters for these tori and we show how we chose the torus parameters for Arcus. Based on the ray-traces we select the position of the CCDs and we present simulations for misalignment in all possible degrees of freedom and use that to build up an error budget. We show that the error budget chosen will degrade  $R$  only by a few percent compared to a perfectly aligned version of Arcus and that the effect of misalignment on  $A_{\text{eff}}$  is small.

## ACKNOWLEDGMENTS

This work was supported in part by NASA and the Smithsonian Astrophysical Observatory (SAO) via subaward SV8-88004 from SAO to MIT, and by the MIT Kavli Institute for Astrophysics and Space Research. The simulations make use of Astropy, a community-developed core Python package for Astronomy,<sup>18,19</sup> numpy,<sup>20</sup> and IPython.<sup>21</sup> Displays are done with mayavi<sup>22</sup> and matplotlib.<sup>23</sup>

## REFERENCES

- [1] Smith, R. K., Ackermann, M., Allured, R., Bautz, M. W., Bregman, J., Bookbinder, J., Burrows, D., Brenneman, L., Brickhouse, N., Cheimets, P., Carrier, A., Freeman, M., Kaastra, J., McEntaffer, R., Miller, J., Ptak, A., Petre, R., and Vacanti, G., “Arcus: an iss-attached high-resolution x-ray grating spectrometer,” in *Space Telescopes and Instrumentation 2014: Ultraviolet to Gamma Ray*, *Proc. SPIE* **9144**, 91444Y–91444Y–12 (June 2014).
- [2] Smith, R. K., Abraham, M. H., Allured, R., Bautz, M., Bookbinder, J., Bregman, J. N., Brenneman, L., Brickhouse, N. S., Burrows, D. N., Burwitz, V., Carvalho, R., Cheimets, P. N., Costantini, E., Dawson, S., DeRoo, C., Falcone, A., Foster, A. R., Grant, C. E., Heilmann, R. K., Hertz, E., Hine, B., Huenemoerder, D., Kaastra, J. S., Madsen, K. K., McEntaffer, R. L., Miller, E. D., Miller, J., Morse, E., Mushotzky, R., Nandra, K., Nowak, M., Paerels, F., Petre, R., Plice, L., Poppenhaeger, K., Ptak, A., Reid, P., Sanders, J., Schattenburg, M. L., Schulz, N., Smale, A., Temi, P., Valencic, L., Walker, S., Willingale, R., Wilms, J., and Wolk, S. J., “Arcus: the x-ray grating spectrometer explorer,” *Proc. SPIE* **9905**, 9905 – 9905 – 7 (2016).
- [3] Smith, R. K., Abraham, M., Allured, R., Bautz, M., Bookbinder, J., Bregman, J., Brenneman, L., Brickhouse, N. S., Burrows, D., Burwitz, V., Cheimets, P. N., Costantini, E., Dawson, S., DeRoo, C., Falcone, A., Foster, A. R., Gallo, L., Grant, C. E., Gnther, H. M., Heilmann, R. K., Hertz, E., Hine, B., Huenemoerder, D., Kaastra, J. S., Kreykenbohm, I., Madsen, K. K., McEntaffer, R., Miller, E., Miller, J., Morse, E., Mushotzky, R., Nandra, K., Nowak, M., Paerels, F., Petre, R., Poppenhaeger, K., Ptak, A., Reid, P., Sanders, J., Schattenburg, M., Schulz, N., Smale, A., Temi, P., Valencic, L., Walker, S., Willingale, R.,

Wilms, J., and Wolk, S. J., “Arcus: exploring the formation and evolution of clusters, galaxies, and stars,” *Proc.SPIE* **10397**, 10397 – 10397 – 11 (2017).

- [4] Brenneman, L. W., Smith, R. K., Bregman, J., Kaastra, J., Brickhouse, N., Allured, R., Foster, A., Wolk, S., Wilms, J., Valencic, L., Willingale, R., Grant, C., Bautz, M., Heilmann, R., Huenemoerder, D., Miller, E., Nowak, M., Schattenburg, M., Schulz, N., Burwitz, V., Nandra, K., Sanders, J., Bookbinder, J., Petre, R., Ptak, A., Smale, A., Burrows, D., Poppenhaeger, K., Costantini, E., DeRoo, C., McEntaffer, R., Mushotzky, R., Miller, J. M., and Temi, P., “The evolution of structure and feedback with arcus,” *Proc.SPIE* **9905**, 9905 – 9905 – 18 (2016).
- [5] Allured, R., McEntaffer, R. L., Hertz, E., Cheimets, P. N., and Smith, R. K., “Optical design considerations and raytracing results for the arcus grating spectrometer concept,” *Proc.SPIE* **9905**, 9905 – 9905 – 9 (2016).
- [6] Günther, H. M., Bautz, M. W., Heilmann, R. K., Huenemoerder, D. P., Marshall, H. L., Nowak, M. A., and Schulz, N. S., “Ray-tracing critical-angle transmission gratings for the x-ray surveyor and explorer-size missions,” *Proc. SPIE* **9905**, 990556–990556–10 (2016).
- [7] Günther, H. M., Cheimets, P. N., Heilmann, R. K., and Smith, R. K., “Performance of a double tilted-rowland-spectrometer on arcus,” *Proc.SPIE* **10397**, 10397 – 10397 – 12 (2017).
- [8] Beuermann, K. P., Bräuninger, H., and Trümper, J., “Aberrations of a facet-type transmission grating for cosmic x-ray and xuv spectroscopy,” *Appl. Opt.* **17**, 2304–2309 (Aug 1978).
- [9] Collon, M. J., Vacanti, G., Günther, R., Yanson, A., Barriere, N., Landgraf, B., Vervest, M., Chatbi, A., Beijersbergen, M. W., Bavdaz, M., Wille, E., Haneveld, J., Koelewijn, A., Leenstra, A., Wijnerle, M., van Baren, C., Miller, P., Krumrey, M., Burwitz, V., Pareschi, G., Conconi, P., and Christensen, F. E., “Silicon pore optics development for athena,” *Proc. SPIE* **9603**, 96030K–96030K–11 (2015).
- [10] Collon, M. J., Ackermann, M., Günther, R., Chatbi, A., Vacanti, G., Vervest, M., Yanson, A., Beijersbergen, M. W., Bavdaz, M., Wille, E., Haneveld, J., Olde Riekerink, M., Koelewijn, A., van Baren, C., Müller, P., Krumrey, M., Burwitz, V., Sironi, G., and Ghigo, M., “Making the athena optics using silicon pore optics,” *Proc. SPIE* **9144**, 91442G–91442G–8 (2014).
- [11] Heilmann, R. K., Ahn, M., Bruccoleri, A., Chang, C.-H., Gullikson, E. M., Mukherjee, P., and Schattenburg, M. L., “Diffraction efficiency of 200-nm-period critical-angle transmission gratings in the soft x-ray and extreme ultraviolet wavelength bands,” *Appl. Opt.* **50**, 1364–1373 (Apr 2011).
- [12] Heilmann, R. K., Bruccoleri, A. R., and Schattenburg, M. L., “High-efficiency blazed transmission gratings for high-resolution soft x-ray spectroscopy,” *Proc. SPIE* **9603**, 960314–960314–12 (2015).
- [13] Heilmann, R. K., Davis, J. E., Dewey, D., Bautz, M. W., Foster, R., Bruccoleri, A., Mukherjee, P., Robinson, D., Huenemoerder, D. P., Marshall, H. L., Schattenburg, M. L., Schulz, N. S., Guo, L. J., Kaplan, A. F., and Schweikart, R. B., “Critical-angle transmission grating spectrometer for high-resolution soft x-ray spectroscopy on the international x-ray observatory,” *Proc. SPIE* **7732**, 77321J–77321J–11 (2010).
- [14] Henke, B. L., Gullikson, E., and Davis, J., “X-ray interactions: photoabsorption, scattering, transmission, and reflection at  $e=50$ -30000 eV,  $z=1$ -92,” *Atomic Data and Nuclear Data Tables* **54**(2), 181–342 (1993).
- [15] Günther, H. M., Frost, J., , and Theriault-Shay, A., “Chandra-marx/marxs: v1.1,” (Jul 2017).
- [16] Günther, H. M., Frost, J., and Theriault-Shay, A., “MARXS: A Modular Software to Ray-trace X-Ray Instrumentation,” *AJ* **154**, 243 (Dec. 2017).
- [17] Allured, R. and McEntaffer, R. T., “Analytical alignment tolerances for off-plane reflection grating spectroscopy,” *Experimental Astronomy* **36**, 661–677 (Dec. 2013).
- [18] Astropy Collaboration, Robitaille, T. P., Tollerud, E. J., Greenfield, P., Droettboom, M., Bray, E., Aldcroft, T., Davis, M., Ginsburg, A., Price-Whelan, A. M., Kerzendorf, W. E., Conley, A., Crighton, N., Barbary, K., Muna, D., Ferguson, H., Grollier, F., Parikh, M. M., Nair, P. H., Günther, H. M., Deil, C., Woillez, J., Conseil, S., Kramer, R., Turner, J. E. H., Singer, L., Fox, R., Weaver, B. A., Zabalza, V., Edwards, Z. I., Azalee Bostroem, K., Burke, D. J., Casey, A. R., Crawford, S. M., Dencheva, N., Ely, J., Jenness, T., Labrie, K., Lim, P. L., Pierfederici, F., Pontzen, A., Ptak, A., Refsdal, B., Servillat, M., and Streicher, O., “Astropy: A community Python package for astronomy,” *A&A* **558**, A33 (Oct. 2013).

- [19] The Astropy Collaboration, Price-Whelan, A. M., Sipőcz, B. M., Günther, H. M., Lim, P. L., Crawford, S. M., Conseil, S., Shupe, D. L., Craig, M. W., Dencheva, N., Ginsburg, A., VanderPlas, J. T., Bradley, L. D., Pérez-Suárez, D., de Val-Borro, M., Aldcroft, T. L., Cruz, K. L., Robitaille, T. P., Tollerud, E. J., Ardelean, C., Babej, T., Bachetti, M., Bakanov, A. V., Bamford, S. P., Barentsen, G., Barmby, P., Baumbach, A., Berry, K. L., Biscani, F., Boquien, M., Bostroem, K. A., Bouma, L. G., Brammer, G. B., Bray, E. M., Breytenbach, H., Buddelmeijer, H., Burke, D. J., Calderone, G., Cano Rodríguez, J. L., Cara, M., Cardoso, J. V. M., Cheedella, S., Copin, Y., Crichton, D., DÁvella, D., Deil, C., Depagne, É., Dietrich, J. P., Donath, A., Droettboom, M., Earl, N., Erben, T., Fabbro, S., Ferreira, L. A., Finethy, T., Fox, R. T., Garrison, L. H., Gibbons, S. L. J., Goldstein, D. A., Gommers, R., Greco, J. P., Greenfield, P., Groener, A. M., Grollier, F., Hagen, A., Hirst, P., Homeier, D., Horton, A. J., Hosseinzadeh, G., Hu, L., Hunkeler, J. S., Ivezić, Ž., Jain, A., Jenness, T., Kanarek, G., Kendrew, S., Kern, N. S., Kerzendorf, W. E., Khvalko, A., King, J., Kirkby, D., Kulkarni, A. M., Kumar, A., Lee, A., Lenz, D., Littlefair, S. P., Ma, Z., Macleod, D. M., Mastropietro, M., McCully, C., Montagnac, S., Morris, B. M., Mueller, M., Mumford, S. J., Muna, D., Murphy, N. A., Nelson, S., Nguyen, G. H., Ninan, J. P., Nöthe, M., Ogaz, S., Oh, S., Parejko, J. K., Parley, N., Pascual, S., Patil, R., Patil, A. A., Plunkett, A. L., Prochaska, J. X., Rastogi, T., Reddy Janga, V., Sabater, J., Sakurikar, P., Seifert, M., Sherbert, L. E., Sherwood-Taylor, H., Shih, A. Y., Sick, J., Silbiger, M. T., Singanamalla, S., Singer, L. P., Sladen, P. H., Sooley, K. A., Sornarajah, S., Streicher, O., Teuben, P., Thomas, S. W., Tremblay, G. R., Turner, J. E. H., Terrón, V., van Kerkwijk, M. H., de la Vega, A., Watkins, L. L., Weaver, B. A., Whitmore, J. B., Woillez, J., and Zabalza, V., “The Astropy Project: Building an inclusive, open-science project and status of the v2.0 core package,” *ArXiv e-prints* (Jan. 2018).
- [20] van der Walt, S., Colbert, S. C., and Varoquaux, G., “The numpy array: A structure for efficient numerical computation,” *Computing in Science & Engineering* **13**(2), 22–30 (2011).
- [21] Pérez, F. and Granger, B. E., “IPython: a system for interactive scientific computing,” *Computing in Science and Engineering* **9**, 21–29 (May 2007).
- [22] Ramachandran, P. and Varoquaux, G., “Mayavi: 3D Visualization of Scientific Data,” *Computing in Science & Engineering* **13**(2), 40–51 (2011).
- [23] Hunter, J. D., “Matplotlib: A 2d graphics environment,” *Computing In Science & Engineering* **9**(3), 90–95 (2007).